Check for updates

A new molecular material as a dopant-free hole-transporting layer for stable perovskite solar cells†

Rui Zhang,‡[a] Jiang-Yang Shao, ‡[b] Bingcheng Yu,[ac] Hongshi Li,[ac] Yu-Wu Zhong, *[b] Jiangjian Shi,[acd] Yanhong Luo,[acd] Huijue Wu,[a] Dongmei Li[acd] and Qingbo Meng *[acde]

In this work, a new small molecular material, 9,9′-(pyrene-1,6-diyldimethylylidene)bis[*N,N,N′,N′*-tetrakis(4-methoxyphenyl)-9*H*-fluorene-2,7-diamine] (PFD), as a hole-transporting layer was designed for perovskite solar cells (PSCs). PFD has a rigid and flat pyrene unit as the central building block and a symmetric structure to increase the conjugation degree for better carrier conductivity. A power conversion efficiency (PCE) of 18.6% was achieved for PSC based on undoped PFD. When spiro-OMeTAD is further introduced on the top of PFD (PFD/spiro-OMeTAD), a PCE of 21.02% was achieved with a steady-state efficiency of 19.92%, revealing that PFD as an interfacial layer could restrain carrier recombination. Unencapsulated devices based on PFD or PFD/spiro-OMeTAD exhibit excellent stability including long-term stability for over 1400 h under ambient condition, and moisture stability under the "Double 60 program" test simultaneously at 60% RH and 60 °C in air. Besides, no obvious degradation was found for the PFD/spiro-OMeTAD device over 200 h under continuous illumination at the maximum power point tracking (MPPT) in N_2 atmosphere. It is thus suggested that PFD could be a promising dopant-free HTM for PSCs, and also acts as an interface layer to suppress the carrier recombination to further improve the device performance.

Introduction

Perovskite solar cells (PSCs) as the rising star of photovoltaic technology have received wide attention due to the excellent photoelectric properties of hybrid perovskite materials. Thus far, the power conversion efficiency (PCE) of PSCs has reached 25.5%; however, its further commercialization is challenging due to stability issues, which cover the stabilities of perovskite materials and device stabilities under moisture, temperature, oxygen, light (UV) and electric field.[1–4] Encapsulation with hydrophobic polymer materials and coverage with an UV-filter film on the device surface could increase the tolerance of PSCs to humidity and UV light damage to some degree.[5] However, device degradation originating from the defects of the perovskite material itself and interface defects is of major concern.[3,6] Defects could trap or scatter charge carriers to reduce carrier mobility, and some charged defects with high mobility under electric field could result in hysteresis and performance degradation under continuous illumination. Interfacial passivation is thus a widely adopted way to improve the device stability.[7,8]

When the n–i–p structure PSC is exposed to ambient conditions, the back interface (hole transport layer/perovskite, HTL/perovskite) is more easily attacked by moisture, in comparison to the front interface (electron transport layer/perovskite). Ideal back interface is not only beneficial for the hole extraction and transportation, but also for defect passivation at the perovskite surface and grain boundaries.[7,8] Different additives have been introduced into precursor solutions (*i.e.* thiourea, guanidinium salt, potassium halide, extra iodide ions, fused ring electron acceptor materials (INIC2, INIC-Th), *etc.*) or anti-solvents (*i.e.* polystyrene, poly-(methylmethacrylate), *etc.*) to improve perovskite crystallinity, prevent ion migration, reduce or eliminate the hysteresis and passivate grain boundaries and perovskite/HTL interface as well.[9–13] In addition, some ultrathin passivation layers between the perovskite and HTL, such as hydrophobic insulating layers (*i.e.* Teflon, fluoro-silane, *etc.*) and two-dimensional (2-D) perovskites were also reported to improve the V_{oc} and cell performance by the

a Energy Materials and Devices, Beijing National Laboratory for Condense Matter Physics, Institute of Physics, Chinese Academy of Sciences, Beijing, 100190, China. E-mail: qbmeng@iphy.ac.cn, dmli@iphy.ac.cn

b Beijing National Laboratory for Molecular Sciences, CAS Key Laboratory of Photochemistry, CAS Research/Education Center for Excellence in Molecular Sciences, Institute of Chemistry, Chinese Academy of Sciences, Beijing, 100190, China. E-mail: zhongyuwu@iccas.ac.cn

c School of Physics Science, University of Chinese Academy of Sciences, Beijing 100049, China

d Songshan Lake Materials Laboratory, Dongguan 523808, China

e Center of Materials Science and Optoelectronics Engineering, University of Chinese Academy of Sciences, Beijing 100049, China

† Electronic supplementary information (ESI) available. See DOI: 10.1039/d0qm01051k

‡ R. Zhang and J.-Y. Shao contributed equally to this work.

interaction between under-coordinated Pb^{2+} and quaternary ammonium salts (*i.e.* phenylethylammonium iodide (PEAI), octylammonium iodide (OAI), *etc.*).[14–17] Remarkably, selecting appropriate HTLs related to the perovskite/HTL interface is of great concern as well.[18]

Spiro-OMeTAD as a well-established hole-transporting material demonstrated excellent device performance; however, its hole conductivity is strongly dependent on *p*-dopants (such as LiTFSI (lithium bistrifluoromethane sulfonimidate), cobalt salt and *tert*-butylpyridine), which have negative impacts on the device stability due to the hygroscopicity.[19] Developing dopant-free HTMs is undoubtedly necessary, and some dopant-free HTMs have been attempted from polymeric, small molecules to inorganic HTMs; up to 22.1% PCE with only 0.37 V of V_{oc} loss has been achieved.[20–25] In the meantime, the graded HTL structure or double-layer HTMs were also reported, which reduced nonradiative loss, provided efficient hole extraction and increased the device stability.[25–27] However, the device performance of dopant-free HTM-based PSCs is still lower than that of spiro-OMeTAD or PTAA-based PSCs, thus more efforts are needed to seek low-cost and effective HTMs.

In this respect, we designed a new small molecular material based on pyrene, fluorene and triphenylamine groups, 9,9′-(pyrene-1,6-diyldimethylylidene)bis[$N,N,N′,N′$-tetrakis(4-methoxyphenyl)-9*H*-fluorene-2,7-diamine] (PFD), for PSCs. When undoped PFD as a HTM was introduced into the device, 18.6% PCE was achieved. Furthermore, when spiro-OMeTAD was continuously introduced on the top of PFD (abbreviated as PFD/spiro-OMeTAD), 21.02% PCE was achieved with a steady-state efficiency of 19.96%, where PFD can be an interfacial layer to restrain the carrier recombination. Typically, the unencapsulated devices based on PFD and PFD/spiro-OMeTAD can basically maintain its initial PCE after being kept over 1400 h under ambient condition, better than the control group with only 64% of its initial PCE retained. In addition, the "Double 60 program" stability test reveals that the devices based on PFD as the HTM without encapsulation can also keep 98% of its initial PCE after being stored simultaneously at 60% RH and 60 °C in the air over 600 min, exhibiting excellent thermal and moisture stability. The operational stability test reveals no obvious degradation for the PFD/spiro-OMeTAD device over 240 h under continuous illumination at the maximum power point tracking (MPPT) in nitrogen atmosphere. This work shows that PFD exhibits a dual function in PSCs, which acts as a promising dopant-free HTM and interface layer.

Results and discussion

Optical and electrochemical properties of the PFD

PFD is based on pyrene as the central building block and fluorene as the linker with triphenylamine, the structure and synthetic route of which are shown in Fig. 1(a). It was synthesized from 1,6-dibromopyrene and confirmed by ^1H, ^{13}C NMR and mass spectra (Fig. S1–S4 in ESI†). Detailed synthetic processes are described in the Experimental section. According to the UV-visible spectra, a relatively strong absorption peak at 383 nm ($\varepsilon_{383\ nm} = 1.018 \times 10^5$ L mol^{-1} cm^{-1}) and a shoulder
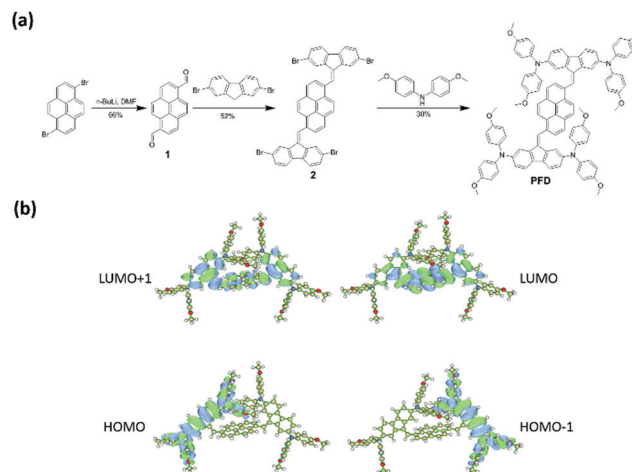

Fig. 1 (a) Molecular structures and synthetic routes to PFD. (b) Optimized geometries and the calculated LUMO/HOMO energy levels of the PFD.

peak at 430 nm ($\varepsilon_{430\ nm} = 3.76 \times 10^4$ L mol^{-1} cm^{-1}) are found, indicating that there is some light absorption for PFD in the visible light range due to the intramolecular charge-transfer transition from the diphenylamine to the pyrene core.[28] Besides, the steady-state photoluminescence (PL) spectrum of PFD shows a maximum emission peak at 532.4 nm. However, no obvious red-shift in absorption peaks can be found for the PFD film, suggesting that there is no obvious π–π interaction between the PFD molecules when they exist in the form of the film (Fig. S5(a), ESI†). According to the UV-visible spectrum and cyclic voltammetry, the bandgap of PFD is 2.39 eV and its highest occupied molecular orbital (HOMO) level was determined to be −5.20 eV, similar to that of spiro-OMeTAD, whereas the lowest unoccupied molecular orbital (LUMO) level of the PFD was calculated to be −2.81 eV, lower than that of spiro-OMeTAD (Fig. S5(b), ESI†).[26] Thermogravimetric analysis (TGA) and differential scanning calorimetry (DSC) indicate that PFD has good thermal stability with a higher decomposition temperature of 435 °C and no obvious glass transition occurs in the temperature range of 50–300 °C (Fig. S6, ESI†). Density functional theory (DFT) calculation was further employed to understand the electronic structure and molecular geometry of PFD at the B3LYP/6-31G(d) level. Its electron density distribution in the highest occupied molecular orbital (HOMO) and the lowest unoccupied molecular orbital (LUMO) is shown in Fig. 1(b). The HOMO is fully delocalized over the 2,7-bis-(diphenylamino)fluorene moiety, whereas the LUMO is mainly located at the central pyrene core and its adjacent fluorene groups. Therefore, for PFD, a rigid and flat pyrene unit is used as the central building block for small-molecule donor materials while a symmetric structure is expected to enhance the conjugation degree, both of which are supposed to be beneficial for carrier conductivity.[28,29]

Interactions between PFD and the perovskite

The morphology of the PFD film on the surface of the perovskite film was first investigated. Here, the perovskite film was adopted as $Cs_{0.04}FA_{0.82}MA_{0.14}Pb(I_{0.87}Br_{0.13})_3$, whose morphology
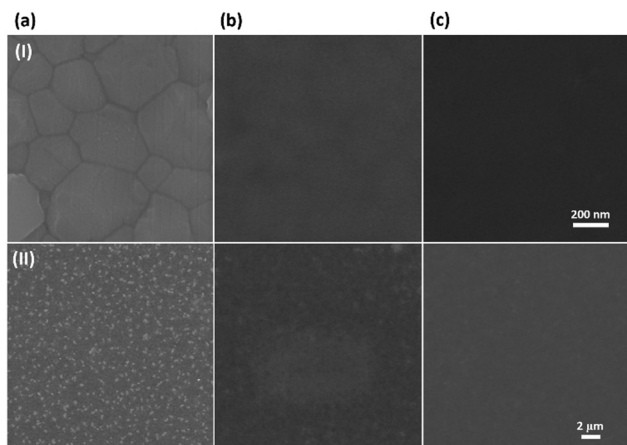
Fig. 2 Top-view SEM images of (a) perovskite (PVSK), (b) PVSK/PFD, and (c) PVSK/spiro-OMeTAD films at two different magnifications (I and II).

is given in Fig. 2(a).[16] The PFD film was obtained by spin-coating its chloroform solution on the top of the perovskite layer at 3000 rpm for 30 s, and then heated at 60 °C for 5 min. Fig. 2(b) and (c) present the surface morphologies of different layers at two magnifications, respectively. We can see that the PFD film (based on 7 mg mL^{-1} concentration) is uniform without pin-holes on the surface of the perovskite; however, much thinner than the spiro-OMeTAD film.

The surface property of the PFD film on the perovskite film was also considered. As we know, the contact angle measurement could reflect the film wetting condition. Here, water contact angles of three films were measured including perovskite (PVSK), PVSK/PFD and PVSK/spiro-OMeTAD. We can see from Fig. 3 that, in comparison with the contact angle of the PVSK film, the contact angle obviously increases when PFD or spiro-OMeTAD is introduced on the perovskite surface; however, a slightly lower value of PFD than that of spiro-OMeTAD is observed, mainly because thinner PFD films do not completely repair the roughness of the perovskite surface (Fig. 2(b) and (c)). Here, we also consider the PVSK/PFD/spiro-OMeTAD composite film, that is, PFD and spiro-OMeTAD are successively deposited on the top of the perovskite, whose contact angle is slightly higher than those of PVSK/PFD and PVSK/spiro-OMeTAD. A similar tendency in the contact angle with glycerol droplets can also be seen for the four films (Fig. S7, ESI†). In order to quantitatively characterize the wetting effects of four films, the surface energy was also estimated by the Owens-Wendt-Rabel-Kaelble (OWRK) method, in which a series of solvents with different surface tensions were employed for contact angles.[30] In this work, four kinds of solvents including water, glycerol, ethylene glycol (EG) and cyclohexane were selected and the liquid/film contact angle of each of them was obtained. According to these contact angles, a linear
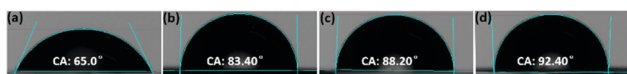
Table 1 Surface energies of the perovskite without or with molecule passivation. Disperse surface energy and polar surface energy are derived from a variety of contact angle measurements by OWRK method

	Disperse σ^d (mN m^{-1})	Total σ^{tot} (mN m^{-1})	Polar σ^p (mN m^{-1})
PVSK	25.14	40.37	15.23
PVSK/PFD	22.85	30.11	7.26
PVSK/spiro-OMeTAD	24.61	28.94	4.33
PVSK/PFD/spiro-OMeTAD	25.88	28.64	2.76

relationship was found between σ_L^d/σ_L^p and the contact angle (θ)-related function using eqn (1):

$$\frac{\sigma_L(\cos\theta + 1)}{2\sqrt{\sigma_L^d}} = \sqrt{\sigma_S^p}\sqrt{\frac{\sigma_L^p}{\sigma_L^d}} + \sqrt{\sigma_S^d} \qquad (1)$$

where σ_L^d is the liquid disperse tension, σ_L^p is the liquid polar tension, and θ is the contact angle, as presented in Fig. S8 (ESI†). Based on fitting data, total surface energies of the four films are given in Table 1. We can see that the PVSK/PFD/spiro-OMeTAD film exhibits the smallest slope, and the slope gradually increases from PVSK/PFD/spiro-OMeTAD, PVSK/spiro-OMeTAD, PVSK/PFD to PVSK films. The perovskite film exhibits the highest surface energy of 40.37 mN m^{-1}; however, for the other three samples, a slight difference in total surface energy is found upon gradual decrease from PVSK/PFD, PVSK/spiro-OMeTAD to PVSK/PFD/spiro-OMeTAD. Particularly, the polar surface energy reduces from 15.23 to 2.76 mN m^{-1}, indicating the surface dipole polarity of the HTM film reduces, which could bring about a decrease in the surface activity of the HTL, such as water adsorption. Obviously, the dopant-free PFD/spiro-OMeTAD composite film exhibits more positive surface dipole polarity, beneficial for the humidity stability.

The AFM images in Fig. 4(I) show that the film roughness can be improved after the HTM is introduced on the perovskite surface (the roughness: 12.7 nm). However, the PFD/PVSK film (roughness: 4.73 nm) is rougher than that of the spiro-OMeTAD/PVSK (roughness: 2.43 nm), which is almost the same as that of PFD/spiro-OMeTAD/PVSK (roughness: 2.61 nm). The relatively rough surface of the PFD/PVSK film is mainly attributed to the thinner PFD layer, which cannot completely repair the roughness of the PVSK film, in good accordance with contact angle measurement results. Besides, the surface potential information of these samples
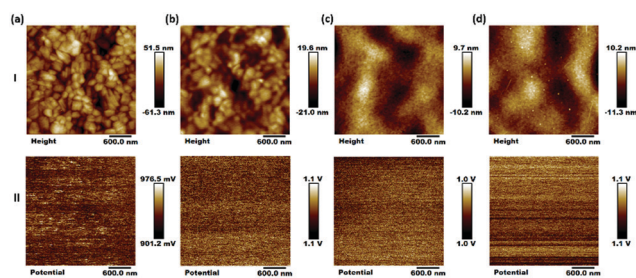

Fig. 4 AFM topographical images (I) and surface potential images (II) of (a) the perovskite (PVSK) film, and composite films (b) PVSK/PFD, (c) PVSK/spiro-OMeTAD, and (d) PVSK/PFD/spiro-OMeTAD.

Fig. 3 Water contact angles of four films: (a) perovskite (PVSK); (b) PVSK/PFD; (c) PVSK/spiro-OMeTAD and (d) PVSK/PFD/spiro-OMeTAD.

was analysed by Kevin probe force microscopy (KPFM) in ambient environment. It can be seen from Fig. 4(II) that the surface potential distribution of the pristine perovskite is basically uniform.[31,32] As we know, the surface potential is related to the surface work function of the tested films, and the work function *vs.* the Au reference is reflected by the contact potential difference (CPD). The CPD value of the perovskite is about 939 mV. When the PFD or spiro-OMeTAD is introduced on perovskite surface films, the HTM films exhibit a similar film forming property. In addition, much narrower surface potential distribution is observed for the three HTM samples.

Carrier dynamic property of PFD

Photoluminescence (PL) spectra were employed to explore the carrier extraction ability of the HTM interfaced with the perovskite. As shown in Fig. 5(a), the PL spectrum of the perovskite at 782 nm is quenched significantly when it is contacted with the PFD, stronger than the spiro-OMeTAD. Time-resolved PL (TRPL) decay also exhibits the fastest carrier recombination of the PFD/perovskite with the average carrier lifetime of 23.08 ns, in comparison with a slower carrier lifetime of 52.89 ns for the spiro-OMeTAD/perovskite, as shown in Fig. 5(b). As we know, the introduction of HTMs into PSCs not only will extract photogenerated holes to favourably arrive at the Au electrode, but it could effectively block the photogenerated electrons from reaching the Au electrode. Although the PFD and spiro-OMeTAD have similar HOMO positions, the lower LUMO level of PFD is disadvantageous to block electrons, thus leading to additional carrier recombination. When PFD is inserted between perovskite and spiro-OMeTAD, more efficient hole extraction can be obtained in comparison to the spiro-OMeTAD/perovskite, suggesting that PFD acts as an interfacial layer to help restrain the recombination.

The hole transportation behaviour of PFD was further evaluated by the space-charge limited current method (SCLC) based on the hole-only single-carrier device with an ITO/PEDOT: PSS/HTM/Au configuration.[33,34] Dark *J–V* curves of the devices are plotted as $\ln[J_d L^3/V^2]$ *vs.* $[V/L]^{0.5}$ (Fig. S9(a) and (b), ESI†) using the following equation:[35]

$$J_d \cong \frac{9\varepsilon_r \varepsilon_0 \mu_h V^2}{8L^3} e^{(0.89\sqrt{V/E_0 L})}$$

where J_d is the dark current, μ_h is the hole mobility, $V = V_{appl} - V_{bi}$ (V_{appl} is the applied bias voltage), L is the HTL thickness, ε_r is the relative dielectric constant of the transport medium, and ε_0 is the vacuum permittivity. Here, ε_r is adopted to be 3 for organic

materials, and ε_0 is 8.85×10^{-12} C V^{-1} m^{-1}. Under the same testing condition, the hole mobility of the undoped PFD was calculated to be 3.65×10^{-5} cm^2 V^{-1} S^{-1} ($d = \sim20$ nm), slightly lower than that of doped spiro-OMeTAD (8.49×10^{-3} cm^2 V^{-1} S^{-1}, $d = \sim200$ nm), however, higher than that of undoped spiro-OMeTAD (4.5×10^{-6} cm^2 V^{-1} S^{-1}).[33] This benefits from the molecular structure of PFD, that is, the introduction of the pyrene core with four fused benzene rings into the PFD, can increase the electron delocalization to obtain an outstanding charge transport ability. In addition, the substitution of the pyrene core by the fluorene linked with triphenylamine branches could give a quasi-two-dimensionally expanded geometry structure, which facilitates the hole mobility by effective delocalization. Besides, based on the linear Ohmic regime, the conductivity of the dopant-free PFD was estimated to be 8.19×10^{-5} S m^{-1}, poorer than that of doped spiro-OMeTAD (4.63×10^{-4} S m^{-1}) (Fig. S9(c) and (d), ESI†).[36]

Photovoltaic properties

Photovoltaic devices are fabricated with a configuration of FTO glass/compact TiO$_2$/[6,6]-phenyl-C61-butyric acid (PCBA)/perovskite/HTM/Au, the cross-sectional SEM image of which is shown in Fig. 6(a). Photocurrent–voltage characteristic (*J–V*) curves of champion cells are displayed in Fig. 6(b). According to the energy levels of the perovskite (VB: ~-5.4 eV) and PFD (HOMO: -5.20 eV), PFD can be used as HTM layer for the PSC.

Fig. 6 (a) Device configuration diagram of the PSC with different energy levels of device materials and the cross-sectional SEM image of the PSC with PFD/spiro-OMeTAD. (b) *J–V* curves of three champion devices with PFD, spiro-OMeTAD and PFD/spiro-OMeTAD. (c) Box statistics diagrams of the efficiencies of PSCs with PFD, spiro-OMeTAD and PFD/spiro-OMeTAD. (d) Output efficiency of the PSC with PFD/spiro-OMeTAD. (e) IPCE spectra of PSCs with PFD, spiro-OMeTAD and PFD/spiro-OMeTAD. Inset: The box statistics diagram of the V_{oc} of corresponding devices.
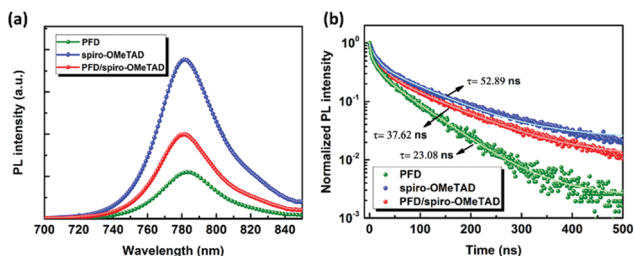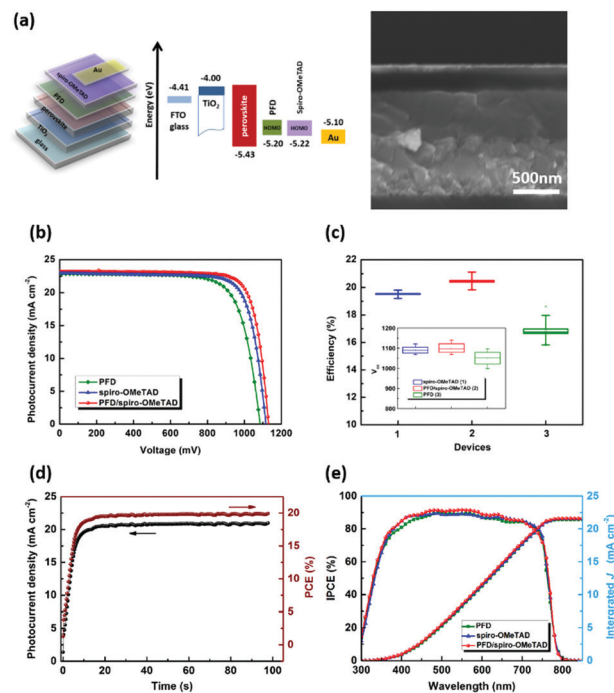

Fig. 5 (a) Steady-state photoluminescence (PL) spectra and (b) time-resolved photoluminescence spectra (TRPL) of the perovskite/HTM on Al$_2$O$_3$ substrates.

Here, the PFD as a dopant-free HTM layer is directly introduced into the device. The PFD thickness can be changed by varying PFD concentrations, and its influence on the cell performance is shown in Table S1 and Fig. S10 (ESI†). We can see that the PFD layer with 7 mg mL^{-1} could present the best cell performance of 18.60% PCE with 22.81 mA cm^{-2} J_{sc}, 1085 mV V_{oc} and 0.751 FF. Under the same fabrication condition, the device with routinely doped spiro-OMeTAD presents an efficiency of 19.79% with 22.98 mA cm^{-2} J_{sc}, 1113 mV V_{oc} and 0.773 FF. The difference between two devices mainly lies in the FF and V_{oc}, probably due to the poor conductivity of PFD. When spiro-OMeTAD is further introduced to cover PFD, the PCE is thus improved to 21.02% with 23.26 mA cm^{-2} J_{sc}, 1131 mV V_{oc} and 0.799 FF. Obviously, much smoother hole extraction is beneficial for obtaining better FF and V_{oc}. In the meantime, the current output at maximum power point (at 950 mV) presents a steady-state efficiency of 19.92%, basically in good agreement with the J–V result (Fig. 6(c)). Statistic histogram of the efficiencies from 50 cells also confirms the variation tendency in the cell performance of three devices and the average V_{oc} is increased by ~20 mV for PFD/spiro-OMeTAD-based PSCs in comparison to spiro-OMeTAD-based PSCs. Corresponding integrated J_{sc} values from the IPCE spectra were also calculated to be 21.42, 21.55 and 21.60 mA cm^{-2} for PFD, spiro-OMeTAD and PFD/spiro-OMeTAD, respectively, as shown in Fig. 6(e).

Investigation on recombination kinetics in the device

To explore the influence of PFD on charge recombination in the device, light intensity–dependent PV measurement was performed. As shown in Fig. 7(a), a linear relationship between the J_{sc} value and the light intensity is observed in double logarithmic plots for the three devices with PFD, spiro-OMeTAD and PFD/spiro-OMeTAD, respectively, indicating that there is no space-charge limit in the TiO$_2$/perovskite/HTM junction.[25] Furthermore, the slopes (α) of fitted lines are 1.16, 1.16 and 1.08 close to 1 for the PSCs with PFD, spiro-OMeTAD and PFD/spiro-OMeTAD, respectively, suggesting that bimolecular recombination occurred in these devices under short-circuit conditions.[25,26] As for a conventional p–n junction solar cell, the open-circuit voltage can be described as $V_{oc} = (nKT/q) \ln(J_{sc}/J_s + 1)$, where J_s is the saturation current density, J_{sc} is the short-circuit photocurrent density, q is the elementary charge, K is Boltzmann's constant, T is the temperature and n is the ideality factor.[25,37] Fig. 7(b) shows the V_{oc} as a function of the logarithm of incident light intensity, which are fitted with a linear function with similar slopes for PFD or spiro-OMeTAD-based PSCs, indicating their similar recombination properties. To further understand the carrier transport and interface properties of the PSCs, electrochemical impedance spectroscopy (EIS) was performed under a voltage bias from 500 to 900 mV in the darkness. As an example, Nyquist plots of the devices at −0.6 V bias voltage in darkness are given in Fig. 7(c). According to Fig. 7(c), the arc is generally contributed by the recombination resistance (R_{rec}) and chemical capacitance of TiO$_2$/perovskite/HTM interfaces. Series resistance (R_s) and R_{rec} of the devices were estimated by fitting the EIS spectra with an appropriate equivalent circuit. As the devices are the same except for using different HTMs, this difference in R_s is mainly related to the HTM resistance (inset of Fig. S11(a), ESI†). Therefore, relatively high R_s of the PFD-based PSC is in good accordance with the unsatisfied hole transportation and lower conductivity of PFD. Besides, the lowest R_s value of the device was obtained when PFD was introduced between the perovskite and spiro-OMeTAD (PFD/spiro-OMeTAD), which is beneficial for a better FF, as shown in Fig. S11(a) (ESI†). To the PSC device, a larger semicircle (R_{rec}) at a higher frequency implies a smaller charge recombination. Under 600 mV bias, the PFD-based device has a larger R_{rec} than the spiro-OMeTAD-based device due to its large conductivity. Besides, when PFD as the interfacial layer was introduced between the perovskite and spiro-OMeTAD, the largest R_{rec} value was obtained, indicating that the existence of PFD can effectively suppress the carrier recombination, in good agreement with the V_{oc} and FF variation tendencies.[38] In the meantime, transient photovoltage measurement reveals that the photovoltage decay lifetime is 0.39 ms for the PFD-based PSC, longer than that for the spiro-OMeTAD-based PSC (0.10 ms).[39] When the spiro-OMeTAD is introduced in PFD-based PSCs, the photovoltage decay lifetime is prolonged to 1.34 ms, suggesting the existence of PFD as an interface layer can suppress the carrier recombination, as shown in Fig. 7(d).

Device stability

To study the influence of PFD on the device stability, different stability testing was carried out.[40,41] First, the PSCs were stored in ambient atmosphere in the darkness without encapsulation, for which the J–V curves were measured under one sun illumination every 10–15 days, as shown in Fig. 8(a). After 1400 h, PSCs based on PFD and spiro-OMeTAD exhibit quite different long-term stability, respectively, that is, no obvious change in the PCE of PFD-based PSCs is found, whereas that of spiro-OMeTAD drops to 64% of its
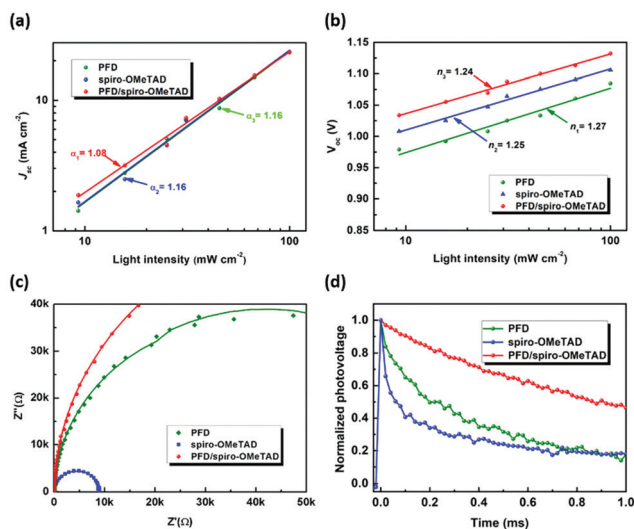

Fig. 7 (a) Short-circuit photocurrent density (J_{sc}) and (b) open-circuit voltage *vs.* incident light intensities. (c) EIS Nyquist plots of PSCs based on PFD, spiro-OMeTAD and PFD/spiro-OMeTAD measured at 600 mV forward bias in the darkness. Symbols: experimental data, Solid line: fitting data. (d) Transient photovoltage spectra of the devices under zero bias voltage in the darkness.
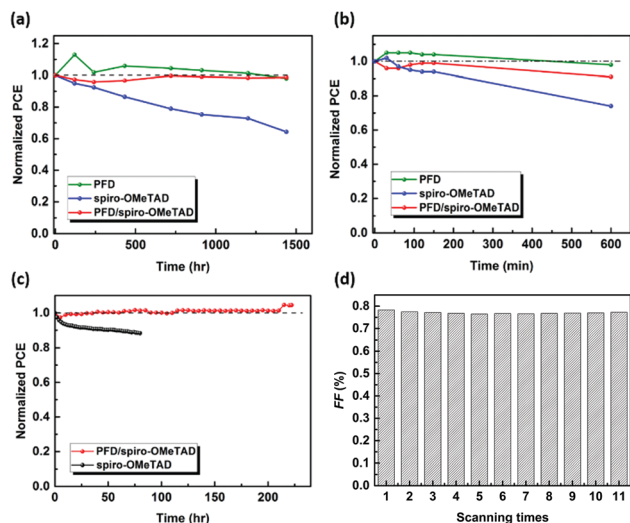
Fig. 8 Stability of unencapsulated PSC devices: (a) long-term stability test; (b) "Double 60 program" moisture stability test; (c) maximum power point tracking (MPPT) stability test of PSCs under light irradiation; and (d) PCEs *versus* multiple scanning times under routine *J*–*V* characteristics.

original PCE. When the spiro-OMeTAD was further deposited on the top of the PFD, this good stability can well be kept, indicating that the dopant-free PFD layer indeed helps to increase the device stability. The "Double 60 program" moisture stability test (simultaneously under 60 °C and 60% RH (relative humidity)) exhibits that this dopant-free PFD can keep 98% of its initial PCE after 600 min testing, while the spiro-OMeTAD-based device only keeps 74% of its initial PCE. To the PFD/spiro-OMeTAD device, 91% of its initial PCE could be retained, as shown in Fig. 8(b). This discrepancy mainly lies in the dopants (*i.e.* LiTFSI) of spiro-OMeTAD, which will raise instability toward humidity when the PSCs are exposed to the environment with a certain humidity. Obviously, the existence of some undoped PFD could increase the anti-humidity ability of the spiro-OMeTAD-based device. Finally, the maximum power point tracking (MPPT) stability test of PSCs under light irradiation, so-called "operational stability test", was attempted. Here, the PSCs were continuously measured at room temperature in N_2 atmosphere under irradiation of AM 1.5 Sun-equivalent, ultraviolet-free white LED lamp and simultaneously at applied bias (maximum power point) for 240 h. The average degradation characteristics are plotted in Fig. 8(c). It is encouraging that no obvious PCE degradation is observed for PFD/spiro-OMeTAD-based PSCs after 240 h testing; however, for spiro-OMeTAD-based PSCs, 88% of its initial PCE is retained after 80 h testing. When the PFD/spiro-OMeTAD-based PSC continuously has *J*–*V* characteristics measured under 100 mW cm^{-2} illumination, the cell performance almost did not change for 11 cycles of testing, suggesting its good illumination stability, as shown in Fig. 8(d) and Fig. S12 (in ESI†).

Experimental

Materials

PbI_2, $PbBr_2$, CH_3NH_3Br (MABr) and $HC(NH_2)_2I$ (FAI) were bought from Xi'An Polymer Light Technology Corp., CH_3NH_3Cl (MACl) from Shanghai MaterWin New Materials Co., Ltd, CsI, bis(trifluoromethane)sulfonimide lithium salt (LiTFSI) and *tert*-butyl pyridine (TBP) from Sigma-Aldrich, dimethyl sulfoxide (DMSO), chlorobenzene, *N*,*N*′-dimethylformide (DMF), titanium isopropoxide and acetonitrile from AlfarAesar, 2,2′,7,7′-tetrakis-[*N*,*N*-di(4-methoxyphenyl)amino]-9,9′-spirobifluorine (spiro-MeOTAD) from Lumtec, tris(2-([1*H*-pyrazol-1-yl]-4-*tert*-butylpyridine))-cobalt(III) tris(bis(trifluoromethyl sulfonyl)imide) (FK209) from Dyesol, $TiCl_4$ from Sinopharm Chemical Reagent Co. Ltd, *n*-butyllithium from J&K Scientific Ltd, and 1,6-dibromopyrene, 2,7-dibromofluorene and di-*p*-anisylamine from Beijing InnoChem Science & Technology Co. Ltd. All the chemicals were directly used without further purification. Before use, laser-patterned FTO glass (sheet resistance: 14 Ω sq^{-1}) was first washed with a mild detergent, rinsed several times with distilled water and subsequently with ethanol in an ultrasonic bath, and finally dried under air stream. Before use, the FTO glass was treated with ultraviolet ozone for 15 min.

Synthesis of PFD

Pyrene-1,6-dicarbaldehyde (1): compound (1) was synthesized by following the procedure reported in the literature.[42] A solution of *n*-butyllithium in hexane (2.6 M, 6 equiv.) was added dropwise to a solution of 1,6-dibromopyrene in anhydrous THF at 0 °C. After the reaction mixture was stirred for 1 h at this temperature, DMF (6 equiv.) was added dropwise to the solution. The mixture was stirred at room temperature for 1 h before water was added. The resulting precipitation was filtered off and washed consecutively with water and methanol to afford the targeted compound 1 (270 mg, 66%).

9,9′-(Pyrene-1,6-diyldimethylylidene)bis(2,7-dibromo-9*H*-fluorene) (2): a suspension of 2,7-dibromofluorene (810 mg, 2.5 mmol), 1 (258 mg, 1.0 mmol), sodium hydroxide (3 mL), and tetramethyl-ammonium bromide (1 mL) in toluene (10 mL) was stirred at 30 °C for 2 h in N_2 atmosphere. The resulting precipitation was filtered off and washed consecutively with water, ethanol and ethyl acetate to afford the targeted compound 2 (450 mg, 52%). MALDI-TOF: 675.1 for $[M]^+$.

9,9′-(Pyrene-1,6-diyldimethylylidene)bis[*N*,*N*,*N*′,*N*′-tetrakis(4-methoxyphenyl)-9*H*-fluorene-2,7-diamine] (PFD): a suspension of di-*p*-anisylamine (137 mg, 0.6 mmol), 2 (87 mg, 0.1 mmol), Pd(OAc)$_2$ (4 mg, 0.02 mmol), P(*t*-Bu)$_3$ (4 mg, 0.02 mmol), and NaO^{t}Bu (60 mg, 0.6 mmol) in toluene (10 mL) was heated at 120 °C for 16 h in N_2 atmosphere in a sealed pressure tube. The system was then cooled to room temperature and the solvent was removed under vacuum. The crude product was purified by silica gel chromatography (eluting with CH_2Cl_2/CH_3OH, 200 : 3) to afford compound PFD (43 mg, yield 30%). MALDI-TOF: 1463.8 for $[M]^+$. ^1H NMR (400 MHz, CDCl$_3$): δ 3.62 (s, 12H), 3.80 (s, 12H), 6.46 (d, *J* = 9.2 Hz, 8H), 6.54 (d, *J* = 8.8 Hz, 8H), 6.69 (s, 2H), 6.86 (d, *J* = 9.2 Hz, 10H), 7.01 (d, *J* = 8.0 Hz, 2H), 7.13 (d, *J* = 8.8 Hz, 8H), 7.37 (d, *J* = 8.4 Hz, 2H), 7.45 (d, *J* = 8.4 Hz, 2H), 7.56 (s, 2H), 7.70 (d, *J* = 8.0 Hz, 2H), 7.88 (d, *J* = 9.2 Hz, 2H), 7.94 (d, *J* = 8.0 Hz, 2H), 8.02 (s, 2H), 8.16 (d, *J* = 8.8 Hz, 2H). ^{13}C NMR (100 MHz, CDCl$_3$): δ 55.32, 55.52, 114.3, 114.6, 114.7, 118.0, 119.2, 121.7, 123.1, 124.5, 124.6, 124.9, 125.4, 125.8,

127.4, 129.0, 130.8, 131.3, 133.6, 137.7, 137.9, 140.4, 140.9, 141.6, 147.2, 147.3, 155.3, 155.5. Anal. calcd for $C_{100}H_{78}N_4O_8$: C, 82.06; H, 5.37; N, 3.83. Found: C, 82.30; H, 5.35; N, 3.80.

Fabrication of perovskite solar cells

First, 20 nm-thickness compact TiO_2 layers were deposited onto a FTO glass substrate by spin-coating 0.125 M titanium isopropoxide sol–gel precursor solution at 3000 rpm, and subsequently calcined at 500 °C for 1 h. The as-prepared TiO_2 films were immersed into 25 mM $TiCl_4$ aqueous solution at 70 °C for 30 min, and finally sintered at 500 °C for 30 min. Then, 0.1 mg mL^{-1} PCBA in chlorobenzene was spin-coated onto the top of TiO_2 compact films.[38,39] Then, a mixed halide perovskite film was obtained by a one-step anti-solvent spin-coating method, that is, 40 μL perovskite precursor solution was dropped onto the TiO_2 layer and spin-coated at 1000 rpm for 10 s and then at 5000 rpm for 30 s, and 120 μL chlorobenzene was poured onto the spinning substrate at 15 s in the second spinning step. The perovskite film was heated at 105 °C for 30 min in the air. The precursor solution consists of 1.37 M PbI_2, 0.20 M $PbBr_2$, 1.29 M FAI and 0.20 M MABr in a DMF/DMSO mixed solvent (v:v = 4:1), and 44 μL CsI-DMSO solution (1.5 M) was subsequently added into the above solution. The precursor solution was thoroughly stirred for 4 h and filtered before use. The HTM layer (undoped PFD in chloroform or spiro-OMeTAD doped with LiTFSI, FK209 and *tert*-butylpyridine (TBP) in chlorobenzene) was deposited onto the top of the perovskite film at 3000 rpm for 30 s and heated at 60 °C for 5 min.[43] Finally, an 80 nm-thickness Au electrode was thermally evaporated on the top of the HTM layer at a pressure of 10^{-7} Torr to complete the device (Kurt J. Lesker).

Characterizations

Surface morphologies of perovskite samples and the cross-sectional image of the device were characterized using a scanning electron microscope (SEM, FEI XL30 S-FEG). Absorption spectra were recorded using a Shimadzu UV-3600 Plus in the wavelength range of 350–850 nm. Thermogravimetric analysis (TGA) was measured using a TA Instruments TGAQ600 at a ramp rate of 10 °C min^{-1} under N_2 flow from 40 to 800 °C. DSC analysis was measured using a DSC Q100 (Du Pont), whose working program was set from 30 to 400 °C at a scan rate of 10 °C min^{-1} for three continuous cycles. Cyclic voltammetry (CV) and differential pulse voltammetry (DPV) measurements were performed using a CHI 660D potentiostat in 0.1 M nBu_4NClO_4 in CH_2Cl_2 using a three-electrode system, in which Ag/AgCl served as the reference electrode, a glassy carbon electrode as the working electrode and a platinum coil as the counter electrode.[33] The working electrode was polished prior to use with 0.05 μm alumina and rinsed thoroughly with water and acetone. The scan rate for CV measurement is 100 mV s^{-1}. Steady-state and time-resolved photoluminescence (PL) spectra were recorded using a PL spectrometer (Edinburgh Instruments, FLS 900) together with a pulsed diode laser (EPL-638.2, 0.8 μJ cm^{-2}) at a pulse frequency of 1 MHz; the excitation wavelength for the PL measurement is 638.2 nm measured at 775 nm after excitation.

In addition, perovskite samples for the PL measurement were deposited onto compact Al_2O_3 substrates. The film thickness (PFD and spiro-OMeTAD) was determined using a surface profiler (P-6, KLA Tech). Atomic force microscopy (AFM) and scanning kelvin probe force microscopy (KPFM) were performed using antimony(n)-doped Si tips (Multimode 8, Bruker) under ambient condition and at room temperature. Photocurrent density–voltage (J–V) characteristics of the cells were recorded using a Keithley 2602 under AM 1.5 irradiation (100 mW cm^{-2}) from SS150-A, Zolix. A black mask with a window of 0.10 cm^2 was clipped on the TiO_2 side to define the active area of the cell. Reverse scanning J–V curves (from open circuit to short circuit) were adopted at a scanning speed of 30 mV s^{-1} with a delay time of 0.3 s. The steady-state output curve of the solar cell was measured at a forward bias around the maximum power point. Incident-photon-to-current conversion efficiency (IPCE) was obtained by a direct current (dc) method on our lab-made IPCE setup under 0.3–0.9 mW cm^{-2} monochromic light illumination.[44] Modulated transient photovoltage (m-TPV) measurement was carried out using our lab-made measuring system, in which the device was excited by 532 nm pulse laser (Opotek, Radiant 355 LD) and the TPV decay process was recorded using a digital oscilloscope (Tektronix, DPO7354C) with a sampling resistor of 50 Ω or 1 MΩ, respectively. A digital signal generator (Tektronix, AFG 3052C) was used to provide an external modulation to the cell, which is connected in parallel to the signal acquisition circuit. A low-pass filter (LPF) with an inductor (for example, 50 H) and a capacitor (for example, 10 μF) was applied to separate the transient electrical signal from the voltage source to avoid shunting the output.[45] Electrochemical impedance spectrum was carried out using a Zahner IM6ex electrochemical workstation in the darkness at an applied bias voltage ranging from 500 to 1000 mV in the frequency range from 1 to 10^6 Hz, and the perturbation amplitude was 10 mV. The as-obtained EIS spectra were fitted using the Z-view software based on an appropriate equivalent circuit.

Conclusion

In this work, we have designed a new small molecular material, 9,9′-(pyrene-1,6-diyldimethylylidene)bis[$N,N,N′,N′$-tetrakis(4-methoxyphenyl)-9H-fluorene-2,7-diamine] (PFD) for PSCs. This PFD layer exhibits better hole mobility than undoped spiro-OMeTAD due to its quasi-two dimensional conjugation structure. PCE of 18.6% has been achieved for the PSCs based on non-doping PFD as the HTM. When spiro-OMeTAD was continuously introduced on the top of the PFD, 21.02% PCE was achieved with a steady-state efficiency of 19.92%. Further research reveals that the PFD can act as an interfacial layer to restrain the carrier recombination. It is found that unencapsulated devices based on PFD or PFD/spiro-OMeTAD exhibit excellent stabilities including long-term stability of being kept over 1400 h under ambient condition, and moisture stability under the "Double 60 program" test simultaneously at 60% RH and 60 °C in the air. In addition, no obvious degradation was found for the PFD/spiro-OMeTAD device over 240 h under continuous illumination at the maximum

power point tracking (MPPT) in nitrogen atmosphere. It is thus suggested that the PFD is a promising dopant-free HTM for PSCs, which also acts as an interface layer to suppress the carrier recombination to improve the device performance.

Author contributions

R. Zhang: Device fabrication and characterization, Draft writing. J.-Y. Shao: Synthesis of PFD and characterization. H. Li: Discussion, Synthesis of perovskite films. B. Yu: KPFM measurement. J. Shi, Y. Luo and H. Wu: Investigation, Experimental discussion. D. Li and Y.-W. Zhong: Supervision, Funding acquisition & Paper reviewing. Q. Meng: Discussion, Funding acquisition & Paper reviewing. The manuscript was completed through contributions of all authors. All authors have given approval to the final version of the manuscript.

Conflicts of interest

There are no conflicts to declare.

Acknowledgements

Notes and references

1 A. Kojima, K. Teshima, Y. Shirai and T. Miyasaka, Organometal halide perovskites as visible-light sensitizers for photovoltaic cells, *J. Am. Chem. Soc.*, 2009, **131**, 6050.

2 https://www.nrel.gov/pv/assets/pdfs/best-research-cell-efficiencies. 20200925.pdf.

3 C. C. Boyd, R. Cheacharoen, T. Leijtens and M. D. McGehee, Understanding degradation mechanisms and improving stability of perovskite photovoltaics, *Chem. Rev.*, 2019, **119**, 3418.

4 Z. Li, C. Xiao, Y. Yang, S. P. Harvey, D. H. Kim, J. A. Christians, M. Yang, P. Schulz, S. U. Nanayakkara, C.-S. Jiang, J. M. Luther, J. J. Berry, M. C. Beard, M. M. Al-Jassim and K. Zhu, Extrinsic ion migration in perovskite solar cells, *Energy Environ. Sci.*, 2017, **10**, 1234.

5 L. Shi, M. P. Bucknall, T. L. Young, M. Zhang, L. Hu, J. Bing, D. S. Lee, J. Kim, T. Wu, N. Takamure, D. R. McKenzie, S. Huang, M. A. Green and A. W. Y. Ho-Baillie, Gas chromatography-mass spectrometry analyses of encapsulated stable perovskite solar cells, *Science*, 2020, **368**, eaba2412.

6 B.-w. Park and S. I. Seok, Intrinsic instability of inorganic–organic hybrid halide perovskite materials, *Adv. Mater.*, 2019, **31**, 1805337.

7 D. Li, J. Shi, Y. Xu, Y. Luo, H. Wu and Q. Meng, Inorganic–organic halide perovskites for new photovoltaic technology, *Natl. Sci. Rev.*, 2018, **5**, 559.

8 J. Shi, X. Xu, D. Li and Q. Meng, Interfaces in perovskite solar cells, *Small*, 2015, **38**, 2472.

9 H. Zhang, J. Shi, L. Zhu, Y. Luo, D. Li, H. Wu and Q. Meng, Polystyrene stabilized perovskite component, grain and microstructure for improved efficiency and stability of planar solar cells, *Nano Energy*, 2018, **43**, 383.

10 D. Luo, W. Yang, Z. Wang, A. Sadhanala, Q. Hu, R. Su, R. Shivanna, G. F. Trindade, J. F. Watts, Z. Xu, T. Liu, K. Chen, F. Ye, P. Wu, L. Zhao, J. Wu, Y. Tu, Y. Zhang, X. Yang, W. Zhang, R. H. Friend, Q. Gong, H. J. Snaith and R. Zhu, Enhanced photovoltage for inverted planar heterojunction perovskite solar cells, *Science*, 2018, **360**, 1442.

11 X. Zheng, B. Chen, J. Dai, Y. Fang, Y. Bai, Y. Lin, H. Wei, X. C. Zeng and J. Huang, Defect passivation in hybrid perovskite solar cells using quaternary ammonium halide anions, *Nat. Energy*, 2017, **2**, 17102.

12 M. Zhang, S. Dai, S. Chandrabose, K. Chen, K. Liu, M. Qin, X. Lu, J. M. Hodgkiss, H. Zhou and X. Zhan, High-performance fused ring electron acceptor-perovskite hybrid, *J. Am. Chem. Soc.*, 2018, **140**, 14938.

13 M. Qin, J. Cao, T. Zhang, J. Mai, T. Lau, S. Zhou, Y. Zhou, J. Wang, Y. Hsu, N. Zhao, J. Xu, X. Zhan and X. Lu, Fused-ring electron acceptor ITIC-Th: a novel stabilizer for halide perovskite precursor solution, *Adv. Energy Mater.*, 2018, **8**, 1703399.

14 Q. Jiang, Y. Zhao, X. Zhang, X. Yang, Y. Chen, Z. Chu, Q. Ye, X. Li, Z. Yin and J. You, Surface passivation of perovskite film for efficient solar cells, *Nat. Photonics*, 2019, **13**, 460.

15 G. Grancini, C. Roldán-Carmona, I. Zimmermann, E. Mosconi, X. Lee, D. Martineau, S. Narbey, F. Oswald, F. De Angelis, M. Grätzel and M. K. Nazeeruddin, One-year stable perovskite solar cells by 2D/3D interface engineering, *Nat. Commun.*, 2017, **8**, 15684.

16 H. Li, J. Shi, J. Deng, Z. Chen, Y. Li, W. Zhao, J. Wu, H. Wu, Y. Luo, D. Li and Q. Meng, Intermolecular π–π conjugation self-assembly to stabilize surface passivation of highly efficient perovskite solar cells, *Adv. Mater.*, 2020, **32**, 1907396.

17 M. Vasilopoulou, A. Fakharuddin, A. G. Coutsolelos, P. Falaras, P. Argitis, A. R. bin, M. Yusoff and M. K. Nazeeruddin, Molecular materials as interfacial layers and additives in perovskite solar cells, *Chem. Soc. Rev.*, 2020, **49**, 4496.

18 Z. Yu and L. Sun, Recent progress on hole-transporting materials for emerging organometal halide perovskite solar cells, *Adv. Energy Mater.*, 2015, **5**, 1500213.

19 W. H. Nguyen, C. D. Bailie, E. L. Unger and M. D. McGehee, Enhancing the hole-conductivity of spiro-OMeTAD without oxygen or lithium salts by using spiro(TFSI)$_2$ in perovskite and dye-sensitized solar cells, *J. Am. Chem. Soc.*, 2014, **136**, 10996.

20 N. Arora, M. I. Dar, A. Hinderhofer, N. Pellet, F. Schreiber, S. M. Zakeeruddin and M. Grätzel, Perovskite solar cells with CuSCN hole extraction layers yield stabilized efficiencies grated than 20%, *Science*, 2017, **358**, 768.

21 X. Yin, J. Zhou, Z. Song, Z. Dong, Q. Bao, N. Shrestha, S. S. Bista, R. L. Ellingson, Y. Yan and W. Tang, Ditheno[3,2-*b*: 2′,3′-*d*]pyrrol-cored hole transport material enabling over

21% efficiency dopant-free perovskite solar cells, *Adv. Funct. Mater.*, 2019, **29**, 1904300.

22 L. Zhang, C. Liu, X. Wang, Y. Tian, A. K. Y. Jen and B. Xu, Side-chain engineering on dopant-free hole-transporting polymers toward highly efficient perovskite solar cells (20.19%), *Adv. Funct. Mater.*, 2019, **29**, 1904856.

23 E. Rezaee, X. Liu, Q. Hu, L. Dong, Q. Chen, J.-H. Pan and Z.-X. Xu, Dopant-free hole transporting materials for perovskite solar cells, *Solar RRL*, 2018, **2**, 1800200.

24 J. Wang, K. Liu, L. Ma and X. Zhan, Triarylamine: Versatile platform for organic, dye-sensitized, and perovskite solar cells, *Chem. Rev.*, 2016, **116**, 14675.

25 Z. Li, J. Park, H. Park, J. Lee, Y. Kang, T. K. Ahn, B.-G. Kim and H. J. Park, Graded heterojunction of perovskite/dopant-free polymeric hole-transport layer for efficient and stable metal halide perovskite devices, *Nano Energy*, 2020, **78**, 105159.

26 M. Abdi-Jalebi, M. I. Dar, S. P. Senanayak, A. Sadhanala, Z. Andaji-Garmaroudi, L. M. Pazos-Outón, J. M. Richter, A. J. Pearson, H. Sirringhaus, M. Grätzel and R. H. Friend, Charge extraction *via* graded doping of hole transport layers gives highly luminescent and stable metal halide perovskite devices, *Sci. Adv.*, 2019, **5**, eaav2012.

27 Q. Li, Y. Zhao, R. Fu, W. Zhou, Y. Zhao, F. Lin, S. Liu, D. Yu and Q. Zhao, Enhanced long-term stability of perovskite solar cells using a double-layer hole transport material, *J. Mater. Chem. A*, 2017, **5**, 14881.

28 J.-Y. Shao, N. Yang, W. Guo, B.-B. Cui, Q. Chen and Y.-W. Zhong, Introducing fluorene into organic hole transport materials to improve mobility and photovoltage for perovskite solar cells, *Chem. Commun.*, 2019, **55**, 13406.

29 A. Krishna and A. C. Grimsdale, Hole transporting materials for mesoscopic perovskite solar cells-towards a rational design?, *J. Mater. Chem. A*, 2017, **5**, 16446.

30 Y. Li, Y. Li, J. Shi, H. Zhang, J. Wu, D. Li, Y. Luo, H. Wu and Q. Meng, High quality perovskite crystals for efficient film photodetectors induced by hydrolytic insulating oxide substrates, *Adv. Funct. Mater.*, 2018, **28**, 1705220.

31 P.-L. Qin, G. Yang, Z.-W. Ren, S. H. Cheung, S. K. So, L. Chen, J. Hao, J. Hou and G. Li, Stable and efficient organo-metal halide hybrid perovskite solar cells *via* π-conjugated Lewis base polymer induced trap passivation and charge extraction, *Adv. Mater.*, 2018, **30**, 1706126.

32 Y. Wang, T. Wu, J. Barbaud, W. Kong, D. Cui, H. Chen, X. Yang and L. Han, Stabilizing heterostructures of soft perovskite semiconductors, *Science*, 2019, **365**, 687.

33 K. Liu, Y. Yao, J. Wang, L. Zhu, M. Sun, B. Ren, L. Xie, Y. Luo, Q. Meng and X. Zhan, Spiro[fluorene-9,90-xanthene]-based hole transporting materials for efficient perovskite solar cells with enhanced stability, *Mater. Chem. Front.*, 2017, **1**, 100.

34 D. Li, J.-Y. Shao, Y. Li, Y. Li, L.-Y. Deng, Y.-W. Zhong and Q. Meng, New hole transporting materials for planar perovskite solar cells, *Chem. Commun.*, 2018, **54**, 1651.

35 P. Cheng, H.-C. Wang, Y. Zhu, R. Zheng, T. Li, C.-H. Chen, T. Huang, Y. Zhao, R. Wang, D. Meng, Y. Li, C. Zhu, K.-H. Wei, X. Zhan and Y. Yang, Transparent hole-transporting frameworks: a unique strategy to design high-performance semi-transparent organic photovoltaics, *Adv. Mater.*, 2017, **29**, 1604758.

36 D. Luo, L. Zhao, J. Wu, Q. Hu, Y. Zhang, Z. Xu, Y. Liu, T. Liu, K. Chen, W. Yang, W. Zhang, R. Zhu and Q. Gong, Dual-source precursor approach for highly efficient inverted planar heterojunction perovskite solar cells, *Adv. Mater.*, 2017, **29**, 1604758.

37 L. J. A. Koster, V. D. Mihailetchi, R. Ramaker and P. W. M. Blom, Light intensity dependence of open-circuit voltage of polymer: fullerence solar cells, *Appl. Phys. Lett.*, 2005, **86**, 123509.

38 H. Li, Y. Li, Y. Li, J. Shi, H. Zhang, X. Xu, J. Wu, H. Wu, Y. Luo, D. Li and Q. Meng, Synergistic effect of caprolactam as Lewis base and interface engineering for efficient and stable planar perovskite solar cells, *Nano Energy*, 2017, **42**, 222.

39 J. Shi, H. Zhang, X. Xu, D. Li, Y. Luo and Q. Meng, Microscopic charge transport and recombination processes behind the photoelectric hysteresis in perovskite solar cells, *Small*, 2016, **38**, 5288.

40 M. Wang, W. Li, X. Gao, W. Yuan, J. Fang, Y. Tao and W. Huang, 35Synthesis of D–π–A–π–D Type Dopant-Free Hole Transporting Materials and Application in Inverted Perovskite Solar Cells, *Acta Chim. Sinica*, 2019, **77**, 741.

41 J. Wu, J. Shi, Y. Li, H. Li, H. Wu, Y. Luo, D. Li and Q. Meng, Quantifying the interface defect for the stability origin of perovskite solar cells, *Adv. Energy Mater.*, 2019, **9**, 1901352.

42 Y. Niko, S. Sasaki, K. Narushima, D. K. Sharma, M. Vacha and G.-I. Konishi, 1,3,6,8-tetrasubstituted asymmetric pyrene derivatives with electron donors and acceptors: high photostability and regioisomer-specific photophysical properties, *J. Org. Chem.*, 2015, **80**, 10794.

43 L. Zhu, Y. Xu, P. Zhang, J. Shi, Y. Zhao, H. Zhang, J. Wu, Y. Luo, D. Li and Q. Meng, Investigation on the role of Lewis based in the ripening process of perovskite films for highly efficient perovskite solar cells, *J. Mater. Chem. A*, 2017, **5**, 20874.

44 X.-Z. Guo, Y.-H. Luo, Y.-D. Zhang, X.-C. Huang, D.-M. Li and Q.-B. Meng, Study on the effect of measuring methods on incident photon-to-electron conversion efficiency of dye-sensitized solar cells by home-made setup, *Rev. Sci. Instrum.*, 2010, **81**, 103106.

45 J. Shi, D. Li, Y. Luo, H. Wu and Q. Meng, Opto-electro-modulated transient photovoltage and photocurrent system for investigation of charge transport and recombination in solar cells, *Rev. Sci. Instrum.*, 2016, **87**, 123107.